Experimental Mechanics (2023) 63:773–789
https://doi.org/10.1007/s11340-023-00942-1

RESEARCH PAPER

Optimal Design, Development and Experimental Analysis of a Tension–Torsion Hopkinson Bar for the Understanding of Complex Impact Loading Scenarios

Y. Xu[1] · J. Zhou[1] · L. Farbaniec[1,2] · A. Pellegrino[1]

Received: 17 August 2022 / Accepted: 23 January 2023 / Published online: 22 March 2023

Abstract

Background Advanced testing methodologies and measurement techniques to identify complex deformation and failure at high strain rates have drawn increasing attention in recent years.

Objective The objective of the current study is the development of a novel combined tension–torsion split Hopkinson bar (TTHB) conceived to generate a combination of tensile and torsional stress waves in a single loading case, and to measure material data representative of real case impact scenarios.

Methods An energy store and release mechanism was employed to generate both the longitudinal and shear waves via the rapid release of a bespoke clamp assembly. A parametric study of the material and geometry of the clamp was implemented via numerical simulations to optimise critical aspects of the wave generation. Thin-walled tube specimens made of two metallic materials were utilised to examine the capability of the developed TTHB system by comparing the experimental measurements with those obtained from conventional split Hopkinson tension and torsion bars.

Results The experimental results demonstrate that the synchronisation of the longitudinal and torsional waves was achieved within 15 microseconds. Different wave rise time were obtained via the controlled release of the clamp using fracture pins of various materials. The analysis indicates that the developed TTHB is capable of characterising the dynamic behaviour of materials under tension, torsion, as well as under a wide range of complex stress states.

Conclusions The presented apparatus, testing and analysis methods allow for the direct population of the dynamic failure stress envelopes of engineering materials and for the accurate evaluation of existing and novel constitutive models.

Keywords Tension–Torsion · Split Hopkinson bar · Wave synchronisation · Von Mises criterion · CP Ti grade 2 · Tension–compression asymmetry

Introduction

The understanding of the physical phenomena governing the response of materials and structures in extreme impact environments is of paramount importance particularly in transportation and defence sectors. During impact loading of aircraft turbine engines, from small-scaled rapid interactions like blade tip rubbing to major events such as bird ingestion or blade containment, the bulk of underlying materials experiences complex stress states and severe plastic deformation at rates of strain that significantly exceed those in normal operations. Such extreme mechanical environments are also experienced in a wide range of engineering applications featuring rapid rebalancing of energy and momentum, such as impact penetration, metal forming and cutting, drilling and blasting, etc. The desire to conceive new engineering materials, to design optimal architectures of engineering systems, and to improve structural integrity, however, is hindered by a lack of data at a broad range of strain rates that could otherwise contribute to either more precisely identifying the existing plasticity models and assess their predicative

✉ Y. Xu
yuan.xu@eng.ox.ac.uk

✉ A. Pellegrino
antonio.pellegrino@eng.ox.ac.uk

[1] Department of Engineering Science, University of Oxford, Parks Road, Oxford OX1 3PJ, UK

[2] Faculty of Physics and Applied Computer Science, AGH University of Science and Technology, Al. Mickiewicza 30, 30-059 Kraków, Poland

capabilities, or developing new models [1, 2]. This challenge has driven more advanced test methodologies and measurement techniques that allow to unravel unknown material properties at high rates of strain and complex stress states.

The split Hopkinson bar (SHB) is the most popular technique to characterise the mechanical behaviour of materials in controlled laboratory environment at a range of high strain rate from 10^2 to 10^4 s^{-1} [3–8]. Since its incipience, SHB has gone through generations of modifications in terms of pulse initiation methods, ambient environment, and measuring instrumentation. Split Hopkinson pressure bar (SHPB) and split Hopkinson tension bar (SHTB) have been successfully employed to characterise the dynamic response and failure of a vast variety of materials under uniaxial loading modes, including metals, polymers, composites, ceramics, and rocks [9–18]. Direct impact of a solid or tubular-like striker bar on the incident Hopkinson bar is the most common approach to generate a longitudinal stress pulse. The method of pulse generation via the impact results in favourably a sharp stress wave with rise time in the order of tenths of microseconds but, inevitably, ringing and Pochammer-Chree oscillations. Therefore, pulse shaping techniques are commonly required, by placing a thin cushion of rubber, tissue, or metal etc., between the striker and the impact face of the incident bar, to filter out high frequency oscillations and diminish dispersion effects. This is essential especially when testing brittle materials as it helps to foster dynamic equilibrium and constant strain rate loading [19, 20]. Furthermore, the duration of the pulse is limited by the length of the striker bar that can be launched. Few attempts were made to generate a tensile wave by quickly releasing an amount of tensile elastic energy that was initially stored in a section of the incident bar [21]. This energy-release approach features easy alteration between tensile and compressive loads and flexible control of the stress pulse duration but requires strict clamping to control the rise time of the pulse and to avoid spurious pulses.

Split Hopkinson torsion bar (SHToB) represents another important branch of the development of the SHB techniques [22–24]. Since the energy-release mechanism remains the main approach to generating stress pulses, special techniques have been proposed to achieve the quick release of the stored energy as it has a direct influence on the quality of the incident wave, especially on the pulse rise time. For example, Pope et al. [25] and Lewis and Goldsmith [26] employed a high voltage capacitor discharge to explode foil and to remove the bonding which clamps the incident bar; this method provides a considerably fast release that results in the wave rise on the order of 1 microsecond. More commonly because of its simplicity and efficiency, the quick release of the clamp can be achieved by the fracture of a notched pin that initially connects the arms of the clamp [23, 24, 27, 28] The wave rise is therefore highly sensitive to the material of the pin and the geometry of the notch. In addition to the energy-release mechanism, explosives [29, 30] that initiated a torsional wave from a transient couple at the flange end of the incident bar seemed a more intuitive way, though strictly simultaneous detonation of two charges was required apart from safety concerns. This approach offered a sharp rise time of the stress wave, typically between 7 and 10 microseconds.

Development of multiaxial Hopkinson bar techniques have received increasing attention in recent years. Although most of the studies are focused on confining techniques [14, 31–35], it does not genuinely provide high-rate loading in multiaxial directions. A few attempts are made to build a true triaxial Hopkinson bar system [36, 37] by installing a cubic specimen in an SHPB system which is additionally modified with four more bars that constrain the remaining faces of the specimen. Three pairs of orthogonal dynamic loads can be achieved by a single longitudinal wave launched by SHPB. This technique is primarily applied to rock and concrete materials yet. Inclination is an ingenious way to achieve compression-induced multiaxial loading by introducing oblique interfaces to either specimens or bar systems [17, 38, 39]. However, the shear load is always dependent of the compression load and limited by the inclination angle. Among the very limited studies of generating multiple stress waves, Lewis and Goldsmith [26] produced a combination of a compressive wave and a torsional wave from two split bars using the above-mentioned impact method and energy-release mechanism, respectively. Triggered by the impact projectile, the clamp was released and its location was chosen so that the two waves propagating at different velocities would arrive at the specimen within ± 10 μs. In the work of Albertini et al. [40], a tensile wave and a shear wave were virtually synchronised by placing a single clamp, which stored both the longitudinal and torsional energies in one bar, sufficiently close to the specimen. However, only a relatively small amount of data was generated with this setup and no further data have been presented since then.

In this study, a new combined tension–torsion split Hopkinson bar (TTHB) system is proposed to reproduce, in a single loading case, the combination of tension and shear (torsion) at high strain rates. The working principle of this combined Hopkinson bar method is elaborated in "Split Tension–Torsion Hopkinson Bar" section , followed by an exhaustive description of critical mechanical designs in "Critical Mechanical Design" section including the clamping technique, wave synchronisation, and wave rise time. Preliminary specimen design is presented in "Experimental Validation" section, which allows for a comparison of the experimental results obtained from TTHB with those from conventional Hopkinson bar techniques, i.e., split Hopkinson tension bar (SHTB) and split Hopkinson torsion bar

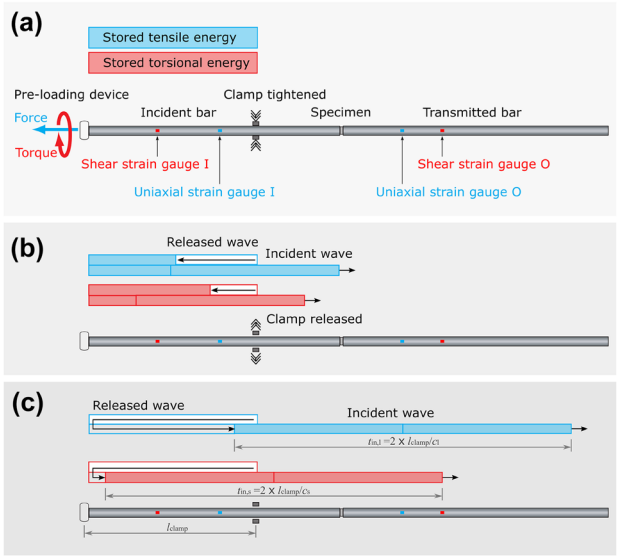

Fig. 1 Schematic of the split tension–torsion Hopkinson bar (TTHB) system and the wave generation mechanism: (**a**) clamp tightened; (**b**) clamp released; and (**c**) continuous wave propagation (wave interactions at the bar-specimen interfaces is not shown)

(SHToB). The whole study is summarised in "Conclusions" section.

Split Tension–Torsion Hopkinson Bar

Working Principle

The mechanical system of the proposed TTHB apparatus, shown schematically in Fig. 1, essentially consists of an incident bar, a transmitted bar, with the testing specimen sandwiched in between, a clamp station, and tension and torsion loading devices. The combined tensile and torsional stress pulses are generated by means of the energy-release mechanism. As shown in Fig. 1(a), by tightening the clamp and then applying force and torque at the distal end of the incident bar, an amount of tensile and torsional energies is stored in the section between the clamp and the loading units. A sudden release of the clamp can initiate a combination of a tensile wave and a torsional wave propagating towards the specimen, termed as the incident tensile and shear waves, respectively. Given conservation of momentum, both waves carry half of the corresponding stored energy. Meanwhile another pair of longitudinal and shear waves of equal magnitudes but opposite signs as the incident waves is generated but travels in the other direction, called the release compressive and shear waves, as shown in Fig. 1(b). Due to the large mechanical impedance of the loading device at the bar end, the released waves reflect back without altering their signs, subsequently counteracting the residual energy in the pre-stressed section, as shown in Fig. 1(c). As the released wave returns to the clamp station, the stored energy would have all released, marking the tail of the incident wave. Therefore, the duration of the generated incident tensile wave $t_{\text{in.l}}$ and shear wave $t_{\text{in.s}}$ is the time required for the longitudinal wave and shear wave (at different wave speeds c_{l} and c_{s}, respectively, see equation (1)) to travel a length equal to twice the pre-stressed section l_{clamp}. Note that the wave interactions at the bar-specimen interfaces are not shown in Fig. 1(c) for the sake of clarity to illustrate the generation of the incident waves. Details of the wave propagation and interaction with the specimen, as well as signal interpretation in a typical TTHB experiment, can be found in [41]. The mechanical design of the pre-loads in tension and torsion is elaborated in [42].

The propagation of the longitudinal wave and shear wave in a long bar can be mathematically expressed as wave equations (1a) and (1b), respectively:

$$\frac{\partial^2 u}{\partial t^2} - c_l \frac{\partial^2 u}{\partial X^2} = 0, c_l = \sqrt{E/\rho} \tag{1a}$$

$$\frac{\partial^2 \theta}{\partial t^2} - c_s \frac{\partial^2 \theta}{\partial X^2} = 0, c_s = \sqrt{G/\rho} \tag{1b}$$

where, u and θ are the linear displacement and the angular displacement, respectively; ∂t and ∂X denote the derivative with regard to time and space, respectively; E, G, and ρ the Young's modulus, shear modulus, and density of the bar material, respectively.

It is worth noting that the shear wave travels at a different speed c_{s}, typically 1.6–1.7 times lower than the longitudinal wave speed c_{l} for a vast majority of the materials. As a result, the shear wave would arrive at the specimen later than the longitudinal wave if using a single clamp to generate both waves, as illustrated in Fig. 1(b). Approximate synchronisation of the two types of waves can be fulfilled by positioning the clamp sufficiently close to the specimen. Another consequence of the different wave velocities is that the duration of the longitudinal wave is shorter than that of the torsional wave, resulting in the effective duration of the combined tension–torsion loading limited by the longitudinal wavelength.

Optimal Design

The axial particle velocity $\dot{u}$ and the angular particle velocity $\dot{\theta}$ of longitudinal and torsional stress waves propagating along a slender rod are given by equations (2a) and (2b).

$$\dot{u} = \frac{\sigma}{\sqrt{\rho E}} \tag{2a}$$

$$\dot{\theta} = \frac{\tau}{r\sqrt{\rho G}} \tag{2b}$$

Table 1 Manufacturer supplied static properties for 7075-T6 aluminium

Density	Elastic modulus	Shear modulus	Poisson's ratio	Tensile strength	Shear strength
ρ	E	G	υ	σ_t	τ
kg/m^3	GPa	GPa	-	MPa	MPa
2810	71.7	26.9	0.33	503	331

where, σ and τ denote the applied stress; r the radius of the bar. Theoretically a higher particle velocity can be achieved by using bars made of high strength lightweight materials, and the maximum strain rate achievable is determined by the yield stress of the material of the bars:

$$\dot{u}_{\max} = \frac{\sigma_Y}{\sqrt{\rho E}} \tag{2c}$$

$$\dot{\theta}_{\max} = \frac{\tau_Y}{r\sqrt{\rho G}} \tag{2d}$$

where, σ_Y and τ_Y, are the yield stress of the bar material. It is worth noting that the stress wave analysis utilised for the evaluation of Hopkinson Bar experiments relies on the stresses in the incident and transmitted bars to be elastic. Therefore, the yield stress of the material of the bars should not be reached but dictates the limit of the force or torque that can be stored without permanent deformations. Hence σ_Y and τ_Y determine the maximum strain rate achievable for a given material of the bars.

Titanium is a kind of material featuring high values of $\sigma_Y/\sqrt{\rho E}$ and $\tau_Y/\sqrt{\rho G}$; however, it is practically difficult to produce a tensile or torsional pulse of an amplitude high enough to benefit from the high yield stress of alloyed titanium. Furthermore, the amount of the stored load is limited by the capacity of the clamp section, and this is generally lower than what the bar material can theoretically withstand [43].

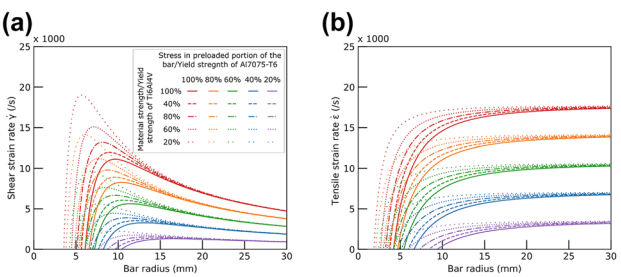

Fig. 2 Variance of the (a) shear strain rate and (b) tensile strain rate with regard to the radius of the bar

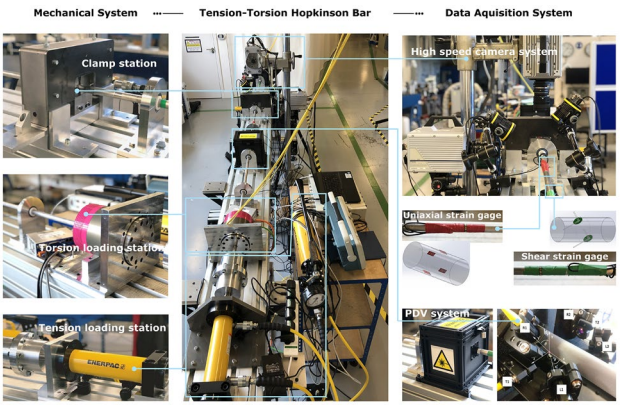

Fig. 3 The TTHB apparatus set up and instrumentation as installed in the Impact Engineering Laboratory at the University of Oxford

It should also be pointed out that, when the same load is stored in bars of equal dimensions, the longitudinal and rotational particle velocities achievable using aluminium are higher than with alloyed titanium, as these are inversely proportional to the density and the elastic moduli of the material (equations (2a) and (2b)). For the above reasons the aluminium alloy 7075-T6 was preferred and selected as the bar material in the present TTHB design, as it allows for higher strain rates to be achieved [21, 26, 43, 44]. The mechanical properties of aluminium alloy 7075-T6 is provided in Table 1.

The diameter of the bar also has considerable influence on the achievable strain rate range. Take the torsional wave loading for instance, the shear strain rate of the specimen can be derived, provided dynamic equilibrium, as:

$$\begin{aligned}\dot{\gamma} = \frac{2}{\rho c_s J}\cdot\frac{r_s}{l_s}\cdot\left(-T_R\right) &= \frac{2}{\rho c_s J}\cdot\frac{r_s}{l_s}\cdot\left(T_I - T_T\right)\\ &= \frac{2}{l_s \rho c_s}\cdot\left(\tau_I\frac{r_s}{r} - \tau_s\frac{J_s}{J}\right).\end{aligned} \tag{3}$$

where, J_s, r_s and l_s are the polar moment of inertia, radius, and gauge length of the specimen, respectively; J is the polar moment of inertia of the bar; TorqueT_I,T_R, and T_T correspond to the amplitude of the incident, reflected, and transmitted shear waves; τ_I and τ_s denote the incident shear stress and the shear strength of the specimen material. Considering the limit condition in which the incident bar approaches its yield point at the pre-stressed section, then the incident shear stress τ_I equals half of the yield strength τ_Y of the bar material,$\tau_I = \tau_Y/2$, which gives:

$$\dot{\gamma} = \frac{2}{l_s \rho c_s}\cdot\left(\frac{\tau_Y r_s}{2r} - \frac{2\tau_s J_s}{\pi r^4}\right) \tag{4}$$

This indicates that the shear strain rate is not monotonically changing with the bar radius. The partial derivative of the shear strain rate with respect to bar radius is derived as equation (5).

Hence, the optimal radius r that allows for a maximum achievable shear strain rate in the specimen can be obtained by setting equation (5) equal to zero, which gives equation (6).

$$\frac{\partial \dot{\gamma}}{\partial r} = \frac{2}{l_s \rho c_s} \cdot \left[\frac{\tau_Y r_s}{2} \left(-\frac{1}{r^2}\right) - \frac{2\tau_s J_s}{\pi} \left(-\frac{4}{r^5}\right) \right] \tag{5}$$

$$r = \sqrt[3]{\frac{16\tau_s J_s}{\pi \tau_Y r_s}} \tag{6}$$

Here we assume the bar material as Al7075-T6 (Table 1) while the test sample is made of Ti6Al4V to show the variation of the strain rate with respect to the bar radius in Fig. 2(a). Typical tensile strength of Ti6Al4V at high-rate is approximately 1200 MPa [45] and the shear strength is thus estimated, assuming Von Mises plasticity as 693 MPa. Figure 2(a) illustrates the variation of the shear strain rate parametrised by the stress amplitude of the incident wave (as a fraction of the yield stress of the bar material Al7075-T6) and the strength of the sample (as a fraction of the strength of Ti6Al4V). It is clear and intuitive that a higher shear strain rate can be achieved given a higher amplitude of the incident wave and a weaker test material. In practice the stored torque generally corresponds to approximately half of the yield point of bar material or lower, due to the above-mentioned difficulty to reach yielding of the bar during experiments. A bar diameter of 20 mm gives a high shear strain rate for a wide range of applications.

Similarly, the tensile strain rate in the specimen can be calculated as:

$$\begin{aligned} \dot{\varepsilon} = \frac{2}{l_s \rho c A} \cdot (-F_R) = \frac{2}{l_s \rho c A} \cdot (F_I - F_T) \\ = \frac{2}{l_s \rho c A} \cdot \left(\frac{\sigma_Y}{2} A - \sigma_s A_s \right) = \frac{2}{l_s \rho c} \cdot \left(\frac{\sigma_Y}{2} - \sigma_s \frac{A_s}{A} \right) \end{aligned} \tag{7}$$

where, A_s and A are the cross section area of the specimen and the bar, respectively. Axial force F_I, F_R, and F_T correspond to the amplitude of the incident, reflected, and transmitted longitudinal waves; σ_s denotes the tensile strength of the specimen material.

As it is always true that $\frac{\partial \dot{\varepsilon}}{\partial r} > 0$, the tensile strain rate monotonically increases with the radius of the bar. The trend considering different amplitudes of the incident wave and test materials is reported in Fig. 2(b). The bar diameter of 20 mm again allows for achieving a high tensile strain rate in a wide range of applications and hence is selected in the present TTHB system.

Instrumentation and Setup

The TTHB system is designed on a commercial profile of a length of 6 m (Fig. 3), to provide a proper alignment of the bars with other mechanical components. The bars are supported by a set of spherical bearings through PTFE (polytetrafluoroethylene) sleeves so that the bar system is self-aligning and free to slide and rotate. The TTHB system is functionally composed of the above-mentioned mechanical system and a data acquisition unit.

A linear hydraulic pump is employed as the pre-tension unit in the tension loading station while a harmonic drive actuator as the pre-torsion device in the torsion loading station. The clamp is optimised to enable a favourable initiation of the combined tensile and torsional waves, as will be elaborated in "Critical Mechanical Design" section.

The data acquisition system includes high-speed camera(s) and lighting unit, photon Doppler velocimetry (PDV), and a set of conventional strain gauges. The high-speed camera system is focused on the specimen to record the footage of the deformation process by means of digital image correlation (DIC) analysis to quantify the full-field deformation. Uniaxial strain gauges and shear strain gauges are located on both the incident bar and the transmitted bar to capture the stress waves, as schematically illustrated in Fig. 1(a). The longitudinal and shear strain gauges on the incident bar were located 180 mm and 1063 mm away from the incident end of the specimen respectively, while the distances between the transmitted end of the specimen and the longitudinal and shear strain gauges on the transmitted bar were 345 mm and 575 mm, correspondingly. The position of the strain gauges was chosen to ensure that strain histories were recorded in locations where strains are uniform across the bars cross-section and to avoid the superimposition with stress waves reflected from the far end of the bars prior to the failure of the specimen. The uniaxial strain gauge station consists of four linear strain gauges aligned along the bar axis and equally spaced along the circumference, such that it measures only the axial stress due to the tensile loading but not due to the potential bending of the bars. Whereas the shear strain gauge station is composed of two T-rosette strain gauges that are aligned along the bar axis by their 45-degree bisector and opposite to each other. The shear strain gauges are wired in such a way to measure only the torsional stress induced by torque. The PDV technique is employed to capture the propagating elastic waves of longitudinal and shear nature and complement the measurements of the strain gauges, therefore improving the reliability of the data acquisition system. Each bar is instrumented with one PDV enclosure for the measurements of longitudinal, rotational, and transverse motions. More details of the PDV techniques in the TTHB apparatus can be found in [46].

Critical Mechanical Design

Clamping-Releasing Mechanism

The design of the clamp plays an essential role in the energy-release mechanism used in this study to generate stress

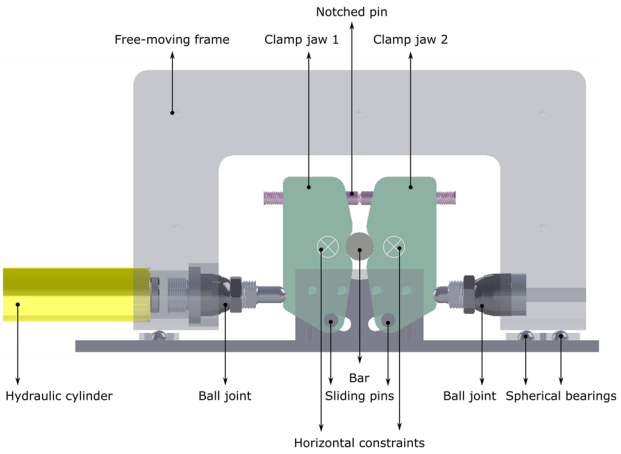

Fig. 4 Schematic of the clamp system

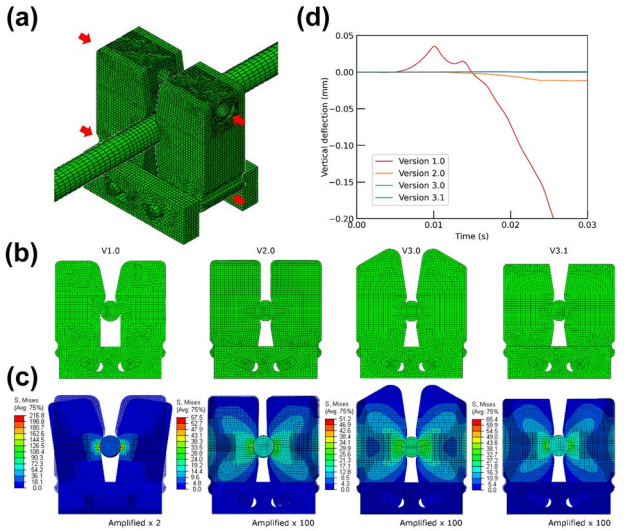

Fig. 5 Parametric study of the geometry of the clamp: (a) finite element model of the clamp assembly; (b) clamp jaws of different geometries; (c) the simulated results; and (d) deflection curve of the bar centroid at the clamped section during clamping

pulses. An ideal design should provide sufficient clamping capacity that prevents the bar from slipping and bending, while on the other hand enable fast and clean release that produces a sharp wave rise and avoids interference from spurious waves due to bar bending. The proposed clamp station is schematically shown in Fig. 4, essentially consisting of a pair of identical clamp jaws that are connected via a notched fracture pin at the top while pressured by a hydraulic cylinder at the bottom. The bar is clamped by increasing the hydraulic pressure not exceeding the fracture load of the pin and then released by further pressure to quickly break the notched pin. A free-moving frame, which is free to slide perpendicular to the bar axis, is designed to allow for equal hydraulic forces applied on both sides of the clamp jaws at the bottom thus preventing transverse movement of the bar in the horizontal plane during clamping. The jaws are attached to a pair of sliding pins at the bottom that guide the jaw to move along a radial slot concentric to the centre of the bar after the breakage of the pin. The jaws are also constrained at the horizontal plane of the bar to prevent the bar from bending in the vertical direction.

The geometry of the jaw is designed to maximise the bar-clamp interaction area that helps increase the gripping capacity without introducing indentation and to prevent vertical deflection of the bar. This part is investigated via finite element (FE) simulations through a non-linear static analysis in ABAQUS/Standard, considering only the initial clamping stage. The FE model of the clamp station without the notched pin is presented in Fig. 5(a). Solid elements C3D8R (ABAQUS/Standard element library, [47]) are used to model the bar, clamp jaws, sliding pins, radial slots, and their interactions. Frictional tangential behaviour is employed in the bar-clamp interaction. The notched fracture pin and the hydraulic cylinder were conceptualised as identical external force demonstrated as the red arrows. Four geometries (Fig. 5(b)) were preliminarily designed by means of a motion analysis to ensure no further interaction between the jaws and the bar during the clamp releasing process. The distribution of von Mises stress and the amplified deflection of the four clamp models are compared in Fig. 5(c). The undeformed model is shaded as a reference to demonstrate the amplified deflection. Particularly the vertical deflection of the bar centroid at the clamp position is extracted in Fig. 5(d). It can be observed that any asymmetry in the load-bearing region of the jaws and in the contact area between the bar and the jaws introduces noticeable vertical deflections (Versions 1.0 and 2.0 in Fig. 5). On the contrary the geometrical symmetry of Versions 3.0 and Version 3.1 results in the absence of any appreciable deflections. Hence Version 3.1 is chosen in the present clamp design as it is exempt from significant deflection of the bar during clamping and undesirable bar-clamp interactions during the clamp releasing process, as confirmed by the experimental data in Fig. 7.

We proceed to assess the influence of the material of the clamp jaws. A more representative FE model is established based on Version 3.1 of the jaw design, as shown in Fig. 6(a). The model of the bar is made of Al7075-T6, 20 mm in diameter and 6 m long, supported by several frictionless bearings. The clamp station is placed at the middle at the bar to reproduce elastic experiments with the incident bar and the transmitted bar connected by an adapter. The notched pin that connects the jaws at the top is modelled since its deformation during the initial clamping stage introduces mechanical asymmetry compared to the direct clamping force at the bottom of the jaws. Clamp jaws made of two materials (aluminium and steel) featuring distinct density, stiffness, and contact friction, are assessed.

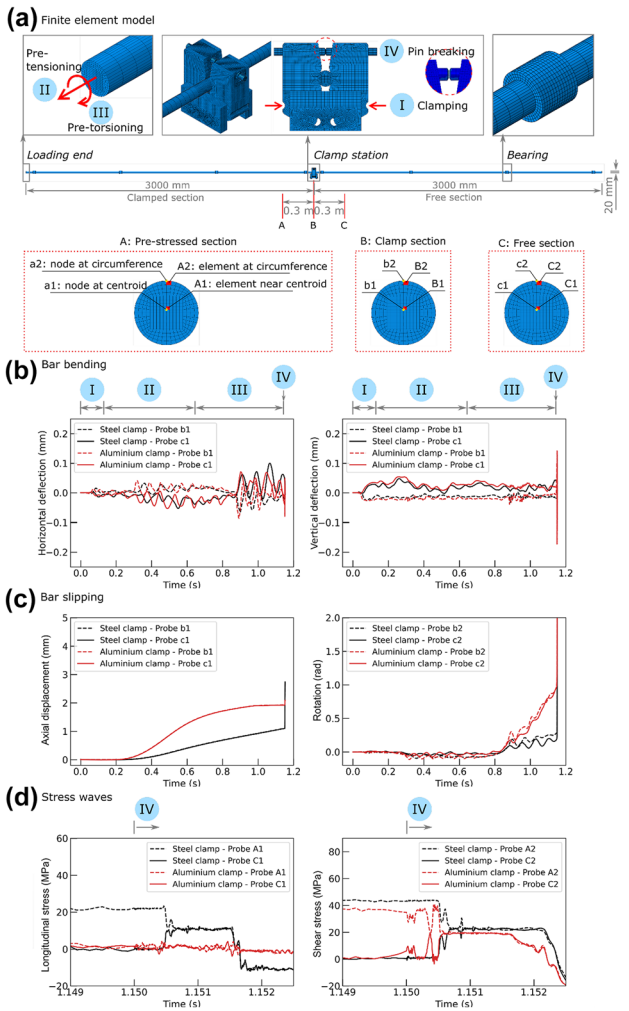

Fig. 6 Parametric study on the material of the clamp: (a) finite element model; (b) bar bending; (c) bar slipping, and (d) the longitudinal and shear waves generated

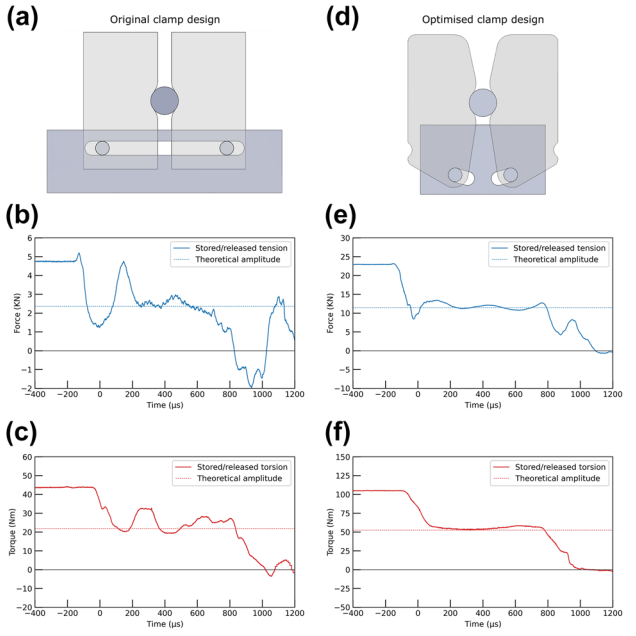

Fig. 7 Experimental validation of the clamp design: (**a**) original clamp design and wave oscillations observed in (**b**) the tensile wave and (**c**) the shear wave; (**d**) optimised clamp design (V3.1) and reduced wave oscillations in (**e**) the tensile wave and (**f**) the shear wave

The whole procedure of a typical TTHB experiment is simulated in ABAQUS/Explicit, to better reproduce the generation and propagation of stress waves. The simulated responses of the bar at three sections A, B, and C (illustrated in Fig. 6(a)) are shown in Figs. 6(b-d) to evaluate possible slippage and bending of the bar, and the subsequently tensile and shear waves generated upon pin snapping. The simulated results obtained from using the steel clamp are presented in black, while those from the aluminium clamp in red. At the three bar sections, i.e., (A) the pre-stressed section, (B) the clamp section, and (C) the free section (Fig. 6(a)), the node and element at the centroid of cross section are used to measure the axial displacement and direct stress, while those at the circumference to probe the rotation and shear stress, respectively. Note that the axial and shear stress at sections A and C after pin breaking can functionally represent the stress waves recorded on the incident and transmitted bar in an actual TTHB experiment.

The horizontal and vertical deflections (Fig. 6(b)) do not show much difference using distinct jaw materials, and both remain at a rather low level due to the optimal geometry design of the jaw. The clamping force was chosen lower than needed to allow potential slipping of the bar during the pre-loading stage, to evaluate the influence of different extents of bar slippage on generating the stress waves. In the case of aluminium clamp, the axial displacement and rotation (Fig. 6(c)) during the first three steps indicate significant longitudinal and rotational slipping of the bar because of the high compliance of the aluminium jaws. As a result, the generated longitudinal stress pulse, if any, oscillates around the zero line (Fig. 6(d)). Even though rotational slipping happened to some extent, a fraction amount of torsional energy was stored, and shear waves are generated but with significant oscillations. In the case of steel jaws, cleaner longitudinal and shear stress waves with a sharp wave rise are generated (Fig. 6(d)). The minor fluctuation can be explained by the slight longitudinal and rotational slipping of the bar during the clamping and energy-storing stage (Fig. 6(c)). It is noted that that after the pin breaks, the shear stress wave generated in the case of aluminium clamp seems to initiate earlier than that using steel clamps due to the larger inertia of the steel clamp. The parametric study of the jaw material indicates that, even though low-density materials would

bring less inertial effect and thus shorten the reaction time by few hundreds of microseconds, high-stiffness materials are preferable as they contribute to reducing bar slippage and generating cleaner stress waves.

The distribution of the stresses across the cross section of the bar was assessed via numerical simulation of stress wave generation events using the Version 3.1 of the clamp. The uniformity of the stresses in the bar was evaluated at cross-sections located between 20 and 100 mm away from the clamp. The modelling results revealed the expected linear distribution of the shear stresses along the radius. The distribution of the longitudinal stresses was essentially uniform, with negligible variations. Even at a distance of 20 mm from the clamp the standard deviation of the longitudinal stress along the radius of the bar was only 0.7% of the mean value. It can therefore be concluded that the current clamp design is capable of generating uniform longitudinal and shear stress waves and that one-dimensional stress wave equations still apply in regions close to the clamp.

The parametric studies on the geometry and material of the clamp presented above lead to steel clamps with geometry Version 3.1 being employed in the current design of TTHB. Elastic experiments were conducted to demonstrate the benefits of the clamp design. Representative waves were recorded from strain gauges on the pre-stressed section of the incident bar, namely the uniaxial strain gauge I and the shear strain gauge I illustrated in Fig. 1(a). The longitudinal wave and the shear wave generated using steel clamp jaws of original and optimised designs are compared in Fig. 7. The initial level of the wave indicates the stored tensile or torsional load, while the first drop marks the release of the clamp, followed by the initiated stress wave that lasts for a duration to travel twice the pre-stressed length of the bar, and finally drops to zero. As illustrated in Fig. 1, the amount of the drop, as well as the amplitude of the incident wave, is in theory equal to half of the stored energy. This theoretical value is marked as a dotted line in Figs. 7(b-c) and (e–f) to evaluate the quality of the stress waves. It is noted that higher force and torque were stored in the bar system using the optimised clamp design to demonstrate its increased capacity.

In all cases, the incident waves showed an average amplitude around the theoretical value calculated from the stored loads. However, some undesirable oscillations can be observed in both the longitudinal and shear waves recorded when using the original clamp (Figs. 7(b) and (c)). Whereas the waves generated by the optimised clamp design appeared smooth and exempt from significant spikes or oscillations (Figs. 7(e) and (f)). The small peak at the beginning of the tensile wave in Fig. 7(e) was attributed to the interaction of the stress wave with the bars-specimen connections. It is also evident, presumably due to different release mechanisms of the stored tensile and torsional energies, that the torsional stress wave appears smoother than the tensile wave. The experimental results demonstrate that the optimised design of the clamp helps minimise the adverse deflection of the bar during the clamping and releasing process thus facilitating a better wave generation. It is also clear that the optimised clamp is capable of storing higher tensile and torsional loads, consequently generating stress waves of higher magnitudes.

Wave Synchronisation

Simultaneous loading of the longitudinal wave and the shear wave on the specimen is another critical requisite in a combined tension–torsion experiment at high strain rates. When using a single clamp to store and release both axial and torsional energies, the time difference between the arrival of the longitudinal and shear waves largely depends on the location of the clamp with respect to the specimen, because of the distinct wave speeds (equations (1a)-(1b)). In the current TTHB design, to minimise the discrepancy in time between the instants the longitudinal wave and the shear wave approach the specimen, the clamp is positioned in immediate proximity to the sample, 40 mm away from the incident bar-specimen interface.

Synchronisation of the waves from three representative combined tension–torsion experiments on commercially pure titanium, titanium 6Al4V alloy, and commercially pure copper specimens is evaluated in Fig. 8. The stress waves were recorded from strain gauges on the transmitted bar, as illustrated by uniaxial strain gauge O and shear strain gauge O in Fig. 1(a), and then shifted in time to the bar-specimen interface according to their locations. Three levels below 50% of the amplitude of the waves were selected to evaluate the time difference of the wave fronts. Provided the wave speeds of an Al7075 bar, the distance of 40 mm between the clamp and the bar-specimen interface causes the shear wave to be delayed of about 5 microseconds with respect to the longitudinal wave. This theoretical value is validated by the experimental results shown in Fig. 8(a) at level 50% and Fig. 8 (b) at level 10% with a reasonable tolerance of 2 microseconds. Although the difference between the arrivals of the stress waves is minimised by the clamp position, this difference may also be affected by the interaction between the stress waves and the specimen-bar connection as well as by the different release mechanisms for axial and torsional stress waves. Hence in practice, the time difference can be slightly larger, or the shear wave could reach the specimen earlier, within few microseconds. It is demonstrated from Fig. 8 that the current location of the clamp allows the tensile and shear stress waves to reach the specimen within 15 microseconds from each other. The synchronisation of the wave front of the longitudinal and shear waves is therefore satisfactory.

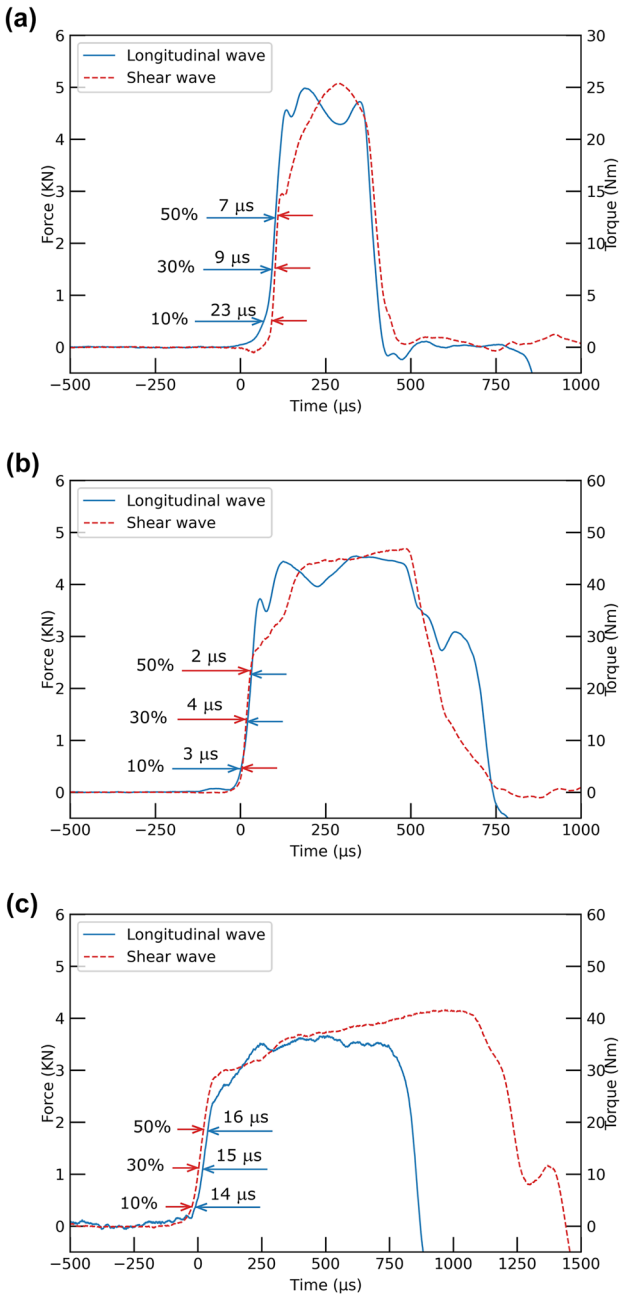

Fig. 8 Difference in time between the instants the longitudinal and shear waves approached the specimen, measured from combined tension–torsion loading experiments of (**a**) commercially pure titanium, (**b**) titanium 6Al4V alloy, and (**c**) commercially pure copper specimens

Wave Rise Time

The clamp release using the pin fracturing mechanism was investigated during experiments where incident and transmitted bars were connected by an impedance matched adapter. Three types of notched pins made from PAI (polyamide-imide), PEEK (polyetheretherketone), and Al7075, characterised by different

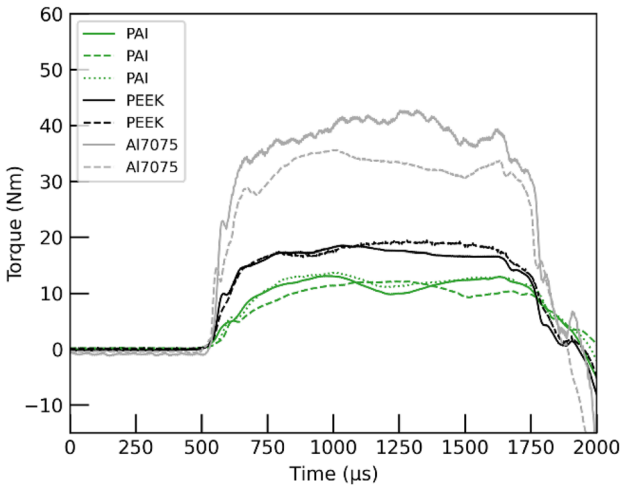

Fig. 9 Influence of the clamp releasing mechanism on the wave rise time measured during experiments conducted using different fracture pins

fracture strains equal to 15%, 10% and 4%, respectively were employed. Shear stress waves measured on the transmitted bar are shown in Fig. 9 as examples. It is worth noting that, as the incident and the transmitted bars were connected by an impedance matched adapter, the stress pulses displayed in Fig. 9 represents, in fact, the incident pulses generated by the elastic energy storage and release mechanism of the apparatus.

The amplitude of the stress waves varied with the stored energy which was limited by the clamping capacity using different notched pins. It is evident that the metallic notched pin can produce stress waves with higher amplitude, whereas the capacity of the composite notched pins appeared lower but can be improved by modifying the geometry of the clamp and the notched pin if needed. More importantly, a gentler wave rise was produced when using PAI pins while a sharper rise was generated using Al7075, the wave rise produced from PEEK falling in between. As the ductility of the notched pin essentially influences the time for the clamp to detach from the bar, the three pin materials represent different clamp detaching period during the clamp release process. On the other hand, the ramped stress wave generated from the ductile fracture of the pin is beneficial for high-rate testing of brittle materials as it facilitates dynamic equilibrium and prevents pre-mature failure [19, 48]. The choice of more ductile pins is therefore equivalent to the use of pulse shaping techniques when the pulse is produced by direct impact.

Experimental Validation

The purpose of this section is to verify the capability of the developed TTHB system to reproduce monotonic tensile load and monotonic torsional load at high strain rates,

and thereafter to obtain compatible engineering tensile and shear stress–strain curves of typical metallic materials. First presented are experimental measurements of two metallic materials subjected to monotonic tension and torsion respectively at high rates of strain using the TTHB system. Their engineering axial stress–strain curves are subsequently compared to those measured from the split Hopkinson tension bar (SHTB), and the shear counterparts compared to those obtained from the split Hopkinson torsion bar (SHToB). Finally, the original and modified von Mises criteria are employed to evaluate the stress locus measured using the TTHB system and the SHTB and SHToB methods.

The geometry of the specimen that allows for appropriate failure under either tensile or torsional loading is still not fully understood. Details on the specimen design are beyond the scope of this study. A preliminary design based on a thin-walled tubular specimen was employed during the experiments.

Experimental Setup and Specimens

Illustrated in Fig. 10 are the SHTB, SHToB, and TTHB methods, and the cylindrical dog-bone specimen, hexagon-ended tubular specimen, and octagon-threaded tubular specimen that suit the different Hopkinson bar methods, respectively. Two metallic materials, commercially pure titanium (CP-Ti) grade 2 and commercially pure copper (Cu, 99.9% purity), are chosen for a series of comparison experiments. The SHTB system employed (Fig. 10(a)) consists of a striker bar, an incident bar, and a transmitted bar, and was designed by Gerlach et al. [49]. The system has been broadly used for dynamic characterisation of metals, polymers, and composites [16, 50, 51] at strain rates ranging from 100 s^{-1} to 3000 s^{-1}. A long U-shape striker made of Ti6Al4V alloy was specially designed to generate long and clean stress pulses free from significant stress oscillations. The SHToB system (Fig. 10b) was initially designed by Campbell et al. [52, 53] using the energy-release mechanism, where the torsional wave is produced via a rapid release of a clamp that pre-stores the torque load. This torsion bar system has been used to characterise the shear responses of metals and composites [16, 53–55] at an achievable shear strain rates of approximately 1000 s^{-1}. Both the incident bar and the transmitted bar are made of Ti6Al4V alloy. The hexagonal ends of the tubular specimen mate with the hexagonal slots on the bars to transmit the torsional waves. The TTHB system (Fig. 10(c) and its working principle have been elaborated in "Working Principle" section. The tension–torsion sample is designed based on the thin-walled tube geometry with octagon-threaded ends to transmit both the longitudinal and torsional waves.

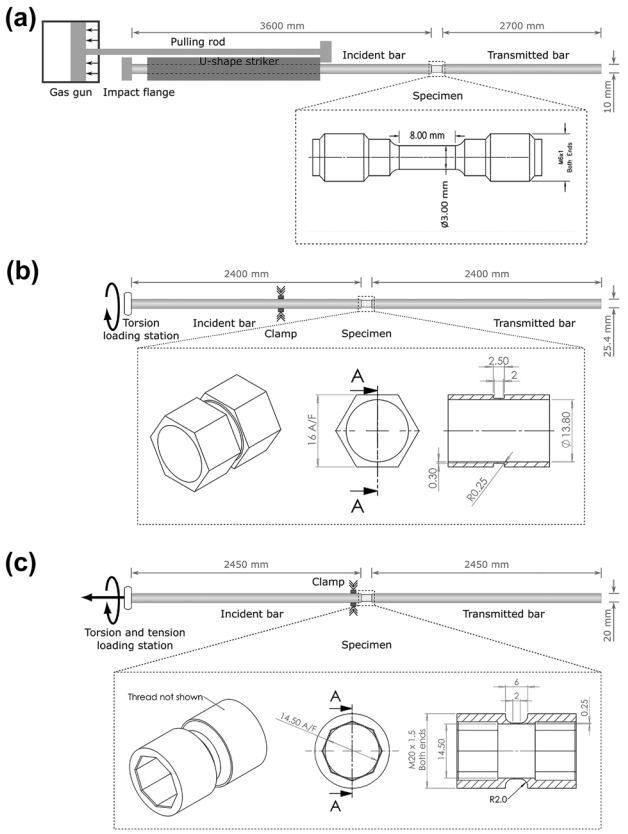

Fig. 10 Graphical illustration of (**a**) the split Hopkinson tension bar (SHTB) and the dog-bone specimen, (**b**) the split Hopkinson torsion bar (SHToB) and the hexagon-ended tubular specimen, and (**c**) the split Hopkinson tension–torsion bar (TTHB) and the octagon-threaded tubular specimen

The generation of stress pulses of considerable duration leads to the unavoidable superimposition of the incident and reflected stress waves. Hence it is not possible, from the measurements of a single strain gauge, to discern the forward and backward travelling waves. As regards the analysis of experiments conducted on the SHTB and SHToB, the forces and torques at the interface between the bars and the sample and the corresponding particle velocities were obtained by placing an additional strain gauge on the incident bar and by separating the incident and reflected waves using the algorithm described in [56, 57]. An alternative wave separation method, based on Photon Doppler velocimetry was previously presented in [58]. The deformation and failure of the samples during SHTB and SHToB experiments, was captured by means of an ultrafast SI Kirana camera. The high-speed footage was recorded with a resolution of 924×748 pixels at a frame rate of 2×10^5 fps and shutter speed of 2 µs.

The use of a wave separation algorithm for the analysis of the experiments conducted on the TTHB requires at least four strain gauges, two for tensile and two for shear strain, positioned on the incident bar. It is also worth noting that the algorithm in [56, 57] is not directly applicable, as all strain gauges are located in the portion of the incident bar between the loading units and the clamp and, therefore, the recorded signals include information on both the initial pre-load and the release of the stress waves. For these reasons, the combined dynamic tensile-shear response of materials tested on the TTHB was determined synchronising the stress history recorded on the transmitted bar and the strain history obtained from digital image correlation analysis on the recorded high-speed footage. This was obtained employing a Photron SA-5 Camera operated at a frame rate of 10^5 fps with a resolution of 256×232 pixels and shutter speed of 2 µs.

Force and torque equilibrium conditions were assessed via direct comparison of the load histories recorded by strain gauges on the incident bar and the ones on the transmitted bar. This is possible because the clamp was positioned in close proximity to the sample. Therefore, the signals recorded on the incident bar correspond, after the initial drop in magnitude subsequent to the release of the clamp, to the superposition of the incident and reflected waves. Hence, their histories represent, starting from the release instant, the load applied on the incident side of the specimen.

A grey-scale speckle pattern was applied to the surface of the specimens to determine the full-field displacement using digital image correlation (DIC) analysis. The mean intensity gradient (MIG) [59, 60] was utilised to evaluate the quality of the speckle pattern. The evaluation gave an average value of 60 calculated from images using the Kirana camera and an average value of 24 of images recorded via the Photron camera. Since MIG values greater than 20 suggest a mean bias error of displacement of less than 1% [59], the high-speed images in this study are characterised by good quality. The excellent MIG value calculated from Kirana images can be attributed to the high resolution of the region of interest and appropriate lighting during the experimentation. The commercial DIC software LaVision Davis[1] was used to calculate the time history of the engineering axial and shear strains within the gauge section.

Experimental Results and Comparison

The typical experimental measurements of CP-Ti subjected to tension at a high strain rate using the TTHB method are presented in Fig. 11. The wave signals recorded from strain gauges at the incident bar and the transmitted bar were converted into force and shifted to the specimen interfaces (Fig. 11(a)). The signal recorded from the incident bar indicated the initially stored load up to 30 KN and the subsequent release of the energy upon clamp opening, while the signal from the transmitted bar depicted wave transmitted through the specimen. The small discrepancy between the loads applied on either end of the specimen implies that dynamic equilibrium of the specimen under high-rate tension was satisfied. This deviation from perfect dynamic equilibrium was ascribed to the interaction of the stress waves with the bars-specimen connections. Additionally, the strain gauge was located within the initially preloaded section of the incident bar, which may also affect slightly the assessment of the dynamic equilibrium conditions. Figure 11(a) also demonstrates the ability of the TTHB system to generate clean tensile waves free from spurious oscillations. Constant strain rate was observed during the plastic flow, calculated from the slope of the strain history as 714 s^{-1} (Fig. 11(b). This further validated the achievement of dynamic equilibrium conditions. The engineering tensile stress–strain curve of CP-Ti (Fig. 11(c)) showed typical plastic characteristics through elastic deformation, slight strain hardening during plastic flow, non-uniform deformation, and finally fracture at the engineering strain of approximately 24%. The DIC analysis showed homogeneous distribution of the axial strain within the gauge section of the specimen during the plastic flow. The strain appeared to localise in the middle of the gauge section approaching the fracture point.

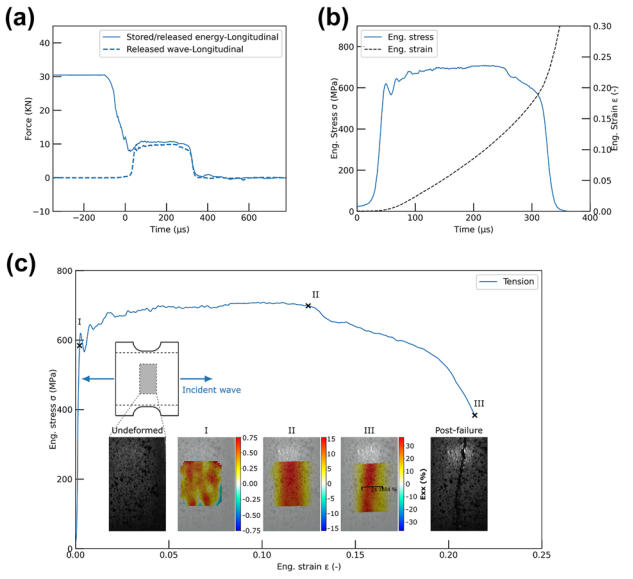

Fig. 11 Typical experimental measurements of CP-Ti subjected to tension at an average strain rate of 714 s^{-1} using the TTHB method: (**a**) dynamic equilibrium; (**b**) time histories of the engineering tensile stress and strain; and (**c**) engineering tensile stress–strain curve and progressive deformation illustrated via DIC

[1] LaVisionUK Ltd, 2 Minton Place Victoria Road, Bicester OX26 6QB, United Kingdom.

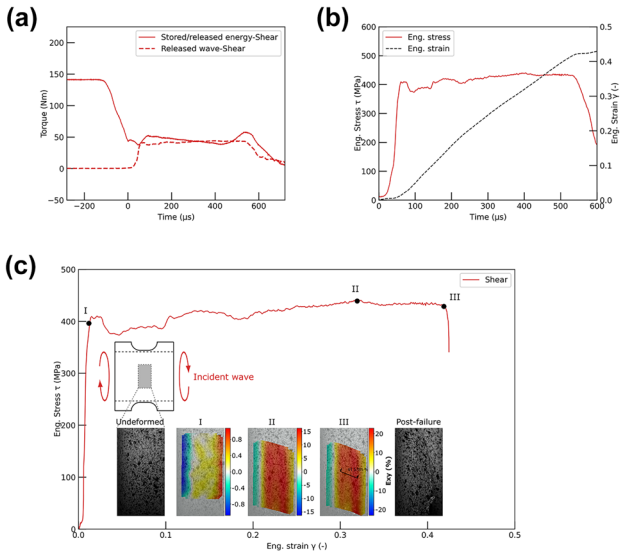

Fig. 12 Typical experimental measurements of CP-Ti subjected to torsion at an average strain rate of 1103 s^{-1} using the TTHB method: (**a**) dynamic equilibrium check; (**b**) time histories of the engineering shear stress and strain; and (**c**) engineering shear stress–strain curve and progressive deformation illustrated via DIC

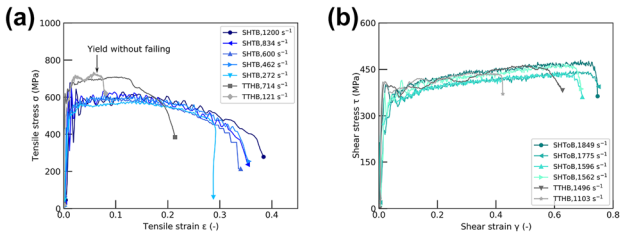

Fig. 13 Comparison of the stress–strain responses of CP-Ti specimens obtained from high-rate (**a**) tensile loading experiments using SHTB and TTHB, and (**b**) torsional loading experiments using SHToB and TTHB

Shown in Fig. 12 are the experimental measurements of CP-Ti subjected to torsion at a high strain rate using the TTHB method. The drop in the initial level of the stored torsional energy indicated the instant at which the clamp was released and the incident wave initiated (Fig. 12(a)). Thereafter the shear wave recorded from the incident bar showed mild oscillations as the specimen started to get engaged with the bars at the beginning of the loading, approximately between 0 μs and 100 μs. After 200 μs the difference between the torque at the two ends of the specimen reduced. Except from the early diversion that may be attributed to the initial slack in the bar-specimen connections, dynamic equilibrium in torsion was reasonably satisfied up to the failure of the specimen. The time histories of stress and strain showed a nearly constant shear strain rate of around 1000 s^{-1} up to fracture, at which the stress started to drop while the strain gradient displayed discontinuity (Fig. 12(b)). The engineering shear stress–strain curve (Fig. 12(c)) showed strain hardening monotonically up to the fracture strain about 41%. Uniform distribution of the circumferential shear strain was shown in the gauge section during the plastic flow. Note that the post-failure images suggested the macroscopic fracture initiated from the other side of the specimen out of the field of the camera. Hence the calculated fracture strain does not reflect the exact engineering shear strain at the fracture onset but provides a good approximation.

In SHTB and SHToB methods, the engineering stress–strain curves of the dog-bone specimen and the hexagon-ended tubular specimen were determined by synchronising the transmitted stress wave and the average strain within the gauge section of the specimens. The tensile flow curves of CP-Ti obtained from the TTHB were then compared with those from the SHTB, while the shear curves from the TTHB compared with those from the SHToB, as shown in Fig. 13(a) and (b), respectively. Overall, the stress–strain responses measured from the TTHB system in both tension and shear are favourably smoother and free from significant oscillations especially at the early stage of deformation.

It is noted that experiments carried out on the different apparatuses were conducted over a range of different strain rates. However, variations in the flow stress of titanium or copper beyond 10^2 s-1 become noticeable only for relatively large differences in the strain rate, as reported in [61, 62]. This consideration allows the comparison of dynamic experiments conducted at different strain rates provided that the response of the investigated materials is not sensitive to those differences. The data obtained from SHTB and SHToB experiments (Fig. 13) show that the flow stress of CP-Ti is not sensitive to the variation of strain rates achieved during dynamic experiments. Similar considerations apply to copper (Fig. 14). TTHB experiments were conducted at strain rates in the same order of magnitude. It is therefore concluded that the comparison of the results obtained on the SHTB, SHToB and TTHB apparatuses is appropriate.

It is worth emphasising that the different Hopkinson Bar apparatuses utilised in this study employ different specimen geometries and that the stress state within the sample is affected by the geometry, even when the sample is deformed under the same loading mode (i.e., tension in TTHB and SHTB, and torsion in TTHB and SHToB).

In torsion the tubular specimens used during TTHB and SHToB experiments have slightly different dimensions, but both approximate a stress state of simple shear. Hence, the nominal shear stress–strain curves measured from different methods are consistent, both in terms of strength and strain to failure (Fig. 13(b)). In both cases, strain hardening was clearly observed up to the macroscopic fracture.

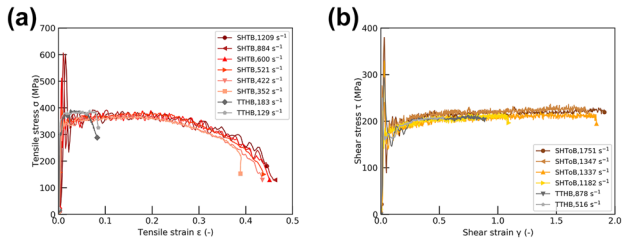

Fig. 14 Comparison of the stress–strain responses of Cu specimens obtained from high-rate (a) tensile loading experiments using SHTB and TTHB, and (b) torsional loading experiments using SHToB and TTHB

In tension, the geometries used during experiments on the TTHB and SHTB apparatuses are substantially different. The stress state induced on a dog-bone specimen approximates the state of uniaxial tension (stress triaxiality $\eta = \sigma_m/\sigma_{vM} = 1/3$, where σ_m and σ_{vM} are the mean stress and von Mises equivalent stress, respectively) whilst the stress state on a tubular sample loaded in tension is approximately a state of plane strain (stress triaxiality $\eta = 1/\sqrt{3}$) in circumferential direction and plane stress in radial direction [63].

Figure 13(a) shows that the fracture strains measured on the TTHB-tubular specimen and on the SHTB-dog-bone sample were in the order of 20% and 30%, respectively, within the range of strains to failure reported in previous studies for CP-Ti grade 2 [1, 64].

It has been shown in the literature that stress triaxiality influences noticeably the fracture strain [63, 65–69]. Several studies have reported the fracture locus of different engineering materials as a function of the stress triaxiality η [63, 65–69], displaying a considerable reduction in the strain to failure from uniaxial tension to plane strain conditions. The smaller fracture strain measured during tension experiments on thin-walled tubular samples agrees with the trends shown in the above literature. Additionally, dog-bone samples tested in uniaxial tension experience significant strain localisation beyond the onset of necking. Conversely, strain localisation is substantially reduced on thin-walled tubular samples, thus resulting in smaller elongation at break.

With regard to the measured strength, the tensile flow stress obtained on thin-walled tubular specimens exceeded the one measured on dog-bone specimens by 16%. This is because the stress state on a thin-walled tubular specimen loaded in tension approximates a state of plane strain in the circumferential direction and of plane stress in the radial direction [63]. The stress state in a dog-bone specimen loaded in tension is, instead, of uniaxial tensile stress. For Levy-von Mises materials, the flow rule yields the stress state within a tubular specimen under direct tension loading as:

$$\boldsymbol{\sigma} = \begin{bmatrix} 0 & 0 & 0 \\ 0 & 0.5\sigma_t & 0 \\ 0 & 0 & \sigma_t \end{bmatrix} \tag{8}$$

where σ_t denotes the axial stress calculated from the axial force over the cross-section area of the tubular specimen. The equivalent stress determined using the von Mises criterion is given by:

$$\sigma_{vM} = \sqrt{3J_2} \tag{9a}$$

where σ_{vM} denotes the von Mises stress, $J_2 = \frac{1}{6}\left[(\sigma_1-\sigma_2)^2 + (\sigma_2-\sigma_3)^2 + (\sigma_3-\sigma_1)^2\right]$ is the second invariant of the stress deviator, and $\sigma_1, \sigma_2, \sigma_3$ are the principal stresses. Considering the stress state of a tubular sample loaded in tension we obtain:

$$\sigma_{vM} = \sqrt{3/4}\sigma_t \tag{9b}$$

Therefore, the tensile stress measured during tensile experiments on tubular specimens is equal to $\sqrt{4/3}$ times the equivalent stress deforming the gauge area of the sample during plastic deformation:

$$\sigma_t = \sqrt{4/3}\sigma_{vM} \tag{9c}$$

Differently, the axial stress measured during tensile loading on dog-bone samples is approximately equal to the equivalent stress deforming the sample. This means that, for the same material, assuming the von Mises criterion, the tensile stress measured on tubular specimens is $\sqrt{4/3}$ times ($\approx 15.5\%$) higher than the uniaxial tensile stress measured on dog-bone specimens. This agrees with the 16% difference between the tensile yield stress measured on the tubular specimens with respect to the yield stress measured on dog-bone specimens.

We conclude that the discrepancy in the tensile stress–strain curves measured using different apparatuses is ascribed to the different stress states associated with different specimen geometries. Tensile loads generate on thin-walled tubular specimens a multiaxial stress state that is different from the uniaxial tensile stress of the dog-bone specimen. Both stress states however contribute to the definition of the failure stress locus of the investigated material and to the description of its behaviour.

We proceed to conduct the same comparison campaign on Cu specimens. The stress–strain curves measured from the TTHB, SHTB, and SHToB method are compared in Fig. 14. In tension (Fig. 14(a)), the tubular specimen fractured at strain of less than 10% which is considerably smaller than that of the dog-bone specimen, of about 40%. A difference of about 13% measured from the yield stress of the tubular specimens over that of the dog-bone specimens was shown, while the ultimate stress was consistent between the two, with a small difference of 1.9%. Similar to CP-Ti (Fig. 13(b)), the shear stress–strain curves of Cu

measured from TTHB and SHToB methods (Fig. 14(b)) are comparable regarding the flow stress and the engineering strain to fracture. The consistency can be again attributed to the comparable tubular geometries of the specimens used in both methods.

It is noted that the fracture strain measured from SHToB experiments varied over a wide range of strains, from 100 to 200%. Given the ductile nature of Cu, the macroscopic fracture can be initiated anywhere on the circumference of the tube, while the rest of the circumference keeps deforming under torsion. It is thus suggested to employ multiple cameras surrounding the circumference of the tubular specimen if the testing space allows, to increase the chance to record the deformation up to fracture onset. This technique has been introduced in quasi-static torsion experiments [41, 55, 70] but remains challenging at high-rate loading due to the limited space in split Hopkinson bar testing and the availability of multiple high-speed cameras.

Ultimate Stress Locus

The measured experimental results using the SHTB, SHToB, and TTHB methods are summarised in the (σ_1, σ_2) plane to depict the ultimate stress loci of CP-Ti and copper under investigation, as shown in Fig. 15. The von Mises criterion and its modified versions are evaluated on the basis of the experimental measurements.

The equation of the original von Mises model is given as equation (9) in "Experimental Results and Comparison" section. There is no predicted effect of hydrostatic stress $\sigma_h = I_1/3$ (where $I_1 = \sigma_1 + \sigma_2 + \sigma_3$ the first stress invariant) in this failure criterion. The pressure dependence was afterwards included in the model by introducing a polynomial term in I_1 [71]:

$$J_2 = k^2 + \sum_{i=1}^{n} \alpha^i I_1^i \tag{10}$$

where, k^2 is a critical value related to the strength of the material, and α^i are constants reflecting the effects of hydrostatic stress. As the pressure dependency introduces a difference in terms of the strength in compression σ_c and tension σ_t, a coefficient m that describes the asymmetry level is introduced as:

$$m = \frac{\sigma_c}{\sigma_t} \tag{11}$$

When $n = 1$ and 2 respectively, equation (10) yields [2, 72, 73]:

$$\sigma_{vM-C} = \frac{1}{2m}\left[(m-1)I_1 + (m+1)\sqrt{3J_2}\right] \tag{12}$$

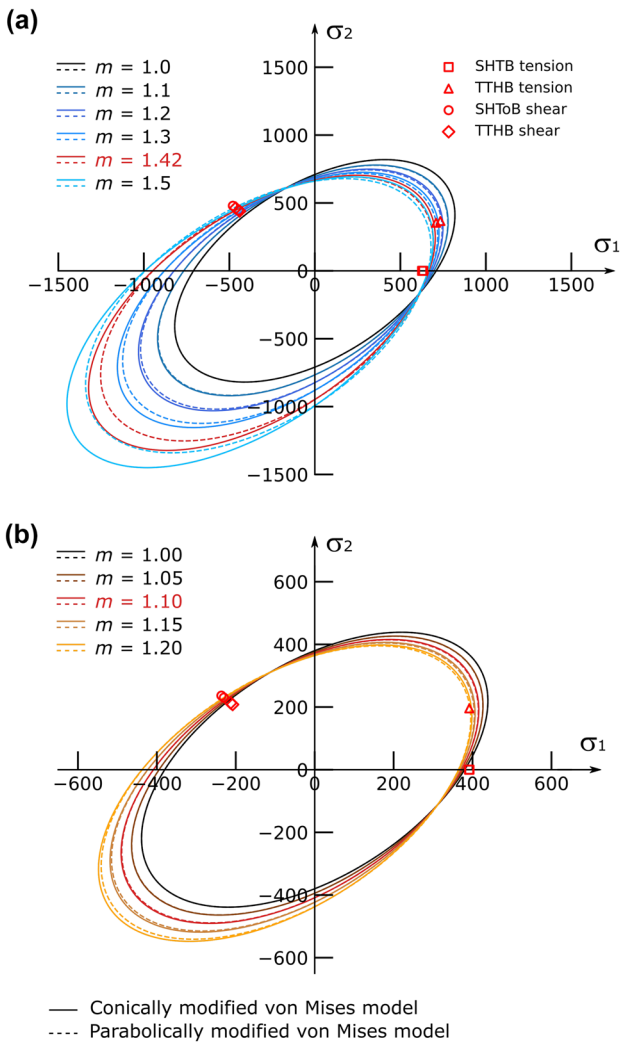

Fig. 15 Projections in the (σ_1, σ_2) plane of the ultimate stress locus of (a) CP-Ti grade 2 and (b) copper, considering the original von Mises criterion, the conically modified von Mises, and the parabolically modified von Mises models under plane stress conditions

$$\sigma_{vM-P} = \frac{m-1}{2m} I_1 + \sqrt{\left(\frac{m-1}{2m} I_1\right)^2 + \frac{3J_2}{m}} \tag{13}$$

Equation 12 is the Drucker-Prager criterion [74], the conically modified von Mises model, which considers the linear effect of I_1; while equation (13) reflects the quadratic effect of I_1, and it is known as the parabolically modified von Mises model.

The von Mises criterion (equation (9)) and its conically and parabolically modified models (equations (12)–(13)) are fitted to the experimental measurements in the (σ_1, σ_2) plane via least square optimisation. Models with different asymmetry levels m are presented. The model that yields the minimum cost is highlighted in red. Figure 15(a) indicates

that CP-Ti grade 2 features a significant level of asymmetry $m = 1.42$. The original von Mises model fails to describe the ultimate stress locus of CP-Ti grade 2, as it overestimates the uniaxial tension measured from SHTB and the plane strain tension from TTHB, but underpredicts the pure shear from SHToB and TTHB. The strong tension–compression asymmetry has been reported for predominantly hexagonal close-packed titanium alloys [1, 75]. As it concerns copper (Fig. 15(b), the original von Mises model well identifies the measured uniaxial tensile strength and pure shear strength but fails to capture the plane strain tension. A level of the tension–compression asymmetry of 1.10 was approximated for copper at the ultimate stress point.

The depicted stress loci show that the TTHB system and the thin-walled tube specimen, by generating monotonic high-rate torsional loading, can reproduce the pure shear stress state as the SHToB method; a plane strain tension stress state, complementary to the uniaxial tensile stress state produced from the dog-bone specimen, can be obtained by generating monotonic high rate tensile loading. Most importantly, as elaborated in sections "Split Tension–Torsion Hopkinson Bar" and "Critical Mechanical Design", the TTHB system can produce simultaneous tensile and torsional loading. Any arbitrary combination of the tension and shear can be reproduced and thus populate the stress locus presented in Fig. 15. In this sense, a wide range of stress states at high rates of strain can be directly measured from a single testing apparatus with identical specimens. This ensures the compatibility of the experimental data while avoiding systematic errors induced by using different testing systems and distinct specimen geometries.

Conclusions

A novel combined tension–torsion split Hopkinson bar (TTHB) apparatus is developed to achieve a combination of tensile and torsional waves in a single loading case. Energy-release mechanism is adopted by using a single clamp to generate both longitudinal and shear waves. The mechanical design of the bar system and the wave initiation mechanism was investigated via finite element modelling and laboratory experiments. Thin-walled tube specimens were employed to verify the capability of the TTHB system by comparison to experimental measurements from conventional split Hopkinson tension bar (SHTB) and split Hopkinson torsion bar (SHToB) apparatuses. The following conclusions can be drawn:

1. The geometry of the clamp is designed to prevent significant deflection of the bar during clamping but also undesirable bar-clamp interactions during the clamp releasing process. The numerical study on the jaw material suggests less inertial effect and fast reaction are obtained when using low-density material. However, high-stiffness material can reduce bar slipping and facilitate the initiation of clean and smooth stress waves.
2. The arrival of the longitudinal and shear waves upon the specimen is determined by the location of the single clamp. It is however also affected by the bar-specimen connection and by the different release mechanisms of the stored tensile and torsional energies. The synchronisation of the wave front of the two waves can be practically satisfied by placing the clamp in close proximity to the bar-specimen interface. In this study, a distance of 40 mm between the clamp and the bar-specimen interface is chosen, and the tensile and shear stress waves reach the specimen within 15 microseconds from each other.
3. A short rise time of the stress wave is the result of a fast release of the clamp, or a quick fracture of the notched pin that connects the clamp jaws. Al7075 notched pins store a larger amount of energy and their brittle fracture can generate stress waves with a sharper wave front, while the ductile fracture of PAI pins extends the detaching time of the clamp from the bar thus increasing the wave rise time, facilitating the obtainment of dynamic equilibrium and preventing the premature failure of brittle specimen materials.
4. The thin-walled tubular specimen under axial tension represents a multiaxial stress state that contributes to depict the stress locus of the investigated material alongside the uniaxial tension measured from SHTB and the pure shear from SHToB. Modified von Mises criteria that consider the effect of the hydrostatic stress approximate better the significant tension–compression asymmetry ($m = 1.42$) of CP-Ti grade 2, and the smaller asymmetry ($m = 1.10$) of copper, at the ultimate stress point.
5. The experimental comparison between the TTHB approach and SHTB and SHToB methods demonstrate the capability of the developed TTHB system to reproduce consistent monotonic tension and monotonic torsion loading, as well as a wide range of stress states at high strain rates. The above comparison ensures the compatibility of the experimental data while avoiding systematic errors induced by using different testing systems and distinct specimen geometries. This, in turn, allows for the accurate evaluation of existing criteria and the development of new material models.

Acknowledgements The authors would like to thank Rolls-Royce plc and the EPSRC for the support under the Prosperity Partnership Grant\ Cornerstone: Mechanical Engineering Science to Enable Aero Propulsion Futures, Grant Ref: EP/R004951/1. The authors are grateful to Mr. S. Carter, Mr. J. Fullerton, Mr. P. Tantrum, and Mr. D. Robinson for their assistance in the manufacturing of the apparatus and specimens, Mrs. K. Bamford for her immense help with procurement, and Dr. David

Townsend and Dr. Longhui Zhang for their help with experiments using the split Hopkinson tension bar and split Hopkinson torsion bar.

Data Availability Raw data were generated at the University of Oxford. The datasets used and analysed during the current study are available from the corresponding authors on reasonable request.

Declarations

Conflict of interest The authors declare that they have no known competing financial interests or personal relationships that could have appeared to influence the work reported in this paper.

References

1. Revil-Baudard B, Cazacu O, Massoni E (2021) Room-temperature plastic behavior and formability of a commercially pure titanium: Mechanical characterization, modeling, and validation. Int J Solids Struct 228:111121
2. Donato GHB, Bianchi M (2012) Pressure dependent yield criteria applied for improving design practices and integrity assessments against yielding of engineering polymers. J Mater Res Technol 1(1):2–7
3. Hopkinson B (1914) A method of measuring the pressure produced in the detonation of high, explosives or by the impact of bullets. Philos Trans R Soc A 213(497–508):437–456
4. Landon JW, Quinney H (1923) Experiments with the Hopkinson pressure bar. Proc R Soc Lond Ser A 103(723):622–643
5. Davies RM (1948) A critical study of the Hopkinson pressure bar. Philos Trans R Soc A 240(821):375–457
6. Kolsky H (1949) An investigation of the mechanical properties of materials at very high rates of loading. Proc Phys Soc 62:676–700
7. Gray III GT (2000) Classic split-Hopkinson pressure bar testing. In H. Kuhn, & D. Medlin (Eds.), *ASM handbook, Mechanical testing and evaluation* (Vol. 8, pp. 1027–1068). ASM International: Materials Park, Ohio
8. Field JE, Walley TM, Proud WG, Goldrein HT, Siviour CR (2004) Review of experimental techniques for high rate deformation and shock studies. Int J Impact Eng 30(7):725–775
9. Krafft JM, Sullivan AM, Tipper CF (1954) The effect of static and dynamic loading and temperature on the yield stress of iron and mild steel in compression. Proc R Soc Lond Ser A 221:114–127
10. Davies EDH, Hunter SC (1963) The dynamic compression testing of solids by the method of the split Hopkinson pressure bar. J Mech Phys Solids 11(3):155–179
11. Harding J, Wood EO, Campbell JD (1960) Tensile testing of materials at impact rates of strain. J Mech Eng Sci 2(2):88–96
12. Harding J, Welsh LM (1983) A tensile testing technique for fibre-reinforced composites at impact rates of strain. J Mater Sci 18(6):1810–1826
13. Nemat-Nasser S, Isaacs JB, Starrett JE (1991) Hopkinson techniques for dynamic recovery experiments. Proc R Soc Lond A 435:371–391
14. Chen W, Ravichandran G (1997) Dynamic compressive failure of a glass ceramic under lateral confinement. J Mech Phys Solid 45(8):1303–1328
15. Tagarielli VL, Deshpande VS, Fleck NA (2008) The high strain rate response of PVC foams and end-grain balsa wood. Compos B Eng 39(1):83–91
16. Pellegrino A, Tagarielli VL, Gerlach R, Petrinic N (2015) The mechanical response of a syntactic polyurethane foam at low and high rates of strain. Int J Impact Eng 75:214–221
17. Xu Y, Dai F (2018) Dynamic response and failure mechanism of brittle rocks under combined compression-shear loading experiments. Rock Mech Rock Eng 51:747–764
18. Zhou J, Pellegrino A, Heisserer U, Duke PW, Curtis PT, Morton J, Petrinic N, Tagarielli VL (2019) A new technique for tensile testing of engineering materials and composites at high strain rates. Proc R Soc Lond Ser A 475(2229):20190310
19. Frew DJ, Forrestal MJ, Chen W (2002) Pulse shaping techniques for testing brittle materials with a split Hopkinson pressure bar. Exp Mech 42(1):93–106
20. Ravichandran G, Chen W (1991) Dynamic failure of brittle materials under uniaxial compression. Experiments in Micromechanics of Fracture Resistant Materials, ed. Kim KS, AMD-130, ASME, New York:85–90
21. Staab GH, Gilat A (1991) A direct-tension split Hopkinson bar for high strain-rate testing. Exp Mech 31:232–235
22. Baker WW, Yew CH (1966) Strain rate effects in the propagation of torsional plastic waves. J Appl Mech 33(6):917–923
23. Hartley KA, Duffy J, Hawley RH (1985) The Torsional Kolsky (Split-Hopkinson) Bar. In 9th ed ASM Handbook, Mechanical Testing (vol. 8, pp. 218–228). American Society for Metals
24. Gilat A (2000) Torsional Kolsky bar testing. In H. Kuhn, & D. Medlin (Eds.), ASM handbook, Mechanical testing and evaluation (Vol. 8, pp. 505–515). ASM International: Materials Park, Ohio.
25. Pope DP, Vreeland T, Wood DS (1964) Machine for producing square torsion pulses of micro-second duration. Rev Sci Instrum 35:1351–1355
26. Lewis JL, Goldsmith W (1975) The dynamic fracture and prefracture response of compact bone by split Hopkinson bar methods. J Biomech 8:27–40
27. Ramesh KT (1994) On the localization of shearing deformations in tungsten heavy alloys. Mech Mater 17(2–3):165–173
28. Peirs J, Verleysen P, Degrieck J (2011) Experimental study of the high strain rate shear behaviour of Ti6Al4V. Appl Mech Mater 82:130–135
29. Duffy J, Campbell JD, Hawley RH (1971) On the use of a torsional split Hopkinson bar to study rate effects in 1100-O Aluminum. J Appl Mech 38:83–91
30. Frantz RA, Duffy J (1972) The dynamic stress-strain behavior in torsion of 1100-O Aluminum subjected to a sharp increase in strain rate. J Appl Mech 39:939–945
31. Forquin P, Gary G, Gatuingt F (2008) A testing technique for concrete under confinement at high rates of strain. Int J Impact Eng 35(6):425–446
32. Frew DJ, Akers SA, Chen W, Green ML (2010) Development of a dynamic triaxial Kolsky bar. Meas Sci Technol 21:105704
33. Hokka M, Black J, Tkalich D, Fourmeau M, Kane A, Hoang NH, Li CC, Chen WW, Kuokkala VT (2016) Effects of strain rate and confining pressure on the compressive be- havior of Kuru granite. Int J Impact Eng 91:183–193
34. Farbaniec L, Hogan JD, Xie KY, Shaeffer M, Hemker KJ, Ramesh KT (2017) Damage evolution of hot-pressed boron carbide under confined dynamic compression. Int J Impact Eng 99:75–84
35. Du HB, Dai F, Xu Y, Yan Z, Wei MD (2020) Mechanical responses and failure mechanism of hydrostatically pressurized

rocks under combined compression-shear impacting. Int J Mech Sci 165:105219
36. Cadoni E, Dotta M, Forni D, Riganti G, Albertini C (2015) First application of the 3D-MHB on dynamic compressive behavior of UHPC. EPJ Web Conf 94:01031
37. Liu K, Zhao J, Wu G, Maksimenko A, Haque A, Zhang QB (2020) Dynamic strength and failure modes of sandstone under biaxial compression. Int J Rock Mech Min Sci 128:104260
38. Zhao PD, Lu FY, Lin YL, Chen R, Li JL, Lu L (2012) Technique for combined dynamic compression–shear testing of PBXs. Exp Mech 52(2):205–213
39. Zhou L, Xu S, Shan J, Liu Y, Wang P (2018) Heterogeneity in deformation of granite under dynamic combined compression/shear loading. Mech Mater 123:1–18
40. Albertini C, Griffiths LJ, Montagnani M, Rodis A, Mariotti P, Paluffi A, Pazienza G (1991) Material characterization by an innovative biaxial shear experiment at very large strains and at very high strain rates. J Phys IV 1(C3):435–440
41. Xu Y, Aceves M, Zhou J, Farbaniec L, Patsias S, Macdougall D, Reed J, Petrinic N, Eakins D, Siviour C, Pellegrino A (2022) Experimental analysis of the multiaxial failure stress locus of commercially pure titanium at low and high rates of strain. Int J Impact Eng 170:104341
42. Xu Y, Farbaniec L, Siviour C, Eakins D. Pellegrino A (2021) The development of split Hopkinson tension-torsion bar for the understanding of complex stress states at high rate. In L. Lamberson, S. Mates, & V. Eliasson (Eds.), Dynamic Behavior of Materials (Vol. 1, pp. 89–93). Conference Proceedings of the Society for Experimental Mechanics Series. Springer, Cham
43. Gilat A, Cheng CS (2000) Torsional split Hopkinson bar tests at strain rates above 104 s^{-1}. Exp Mech 40(1):54–59
44. Espinosa HD, Patanella A, Fischer M (2000) A novel dynamic friction experiment using a modified Kolsky bar apparatus. Exp Mech 40(2):138–153
45. Gour G, Thomson D, Reed J, Petrinic N, Pellegrino A (2021) The effect of strain history on dynamic necking in titanium alloys, experimental and numerical analysis. EPJ Web Conf 250:01032
46. Farbaniec L, Xu Y, Zhou J, Patsias S, Macdougall D, Reed J, Petrinic N, Siviour C, Pellegrino A, Eakins DE (2021) Application of the photon doppler velocimetry (PDV) technique in tension-torsion Hopkinson bar experiments. EPJ Web Conf 250:01025
47. Abaqus (2014) User manuals Version 6.14, Simulia, Providence, USA.
48. Xu Y, Dai F, Xu N, Zhao T (2016) Numerical investigation of dynamic rock fracture toughness determination using a semi-circular bend specimen in split Hopkinson pressure bar testing. Rock Mech Rock Eng 49:731–745
49. Gerlach R, Kettenbeil C, Petrinic N (2012) A new split Hopkinson tensile bar design. Int J Impact Eng 50:63–67
50. Zhang L, Pellegrino A, Townsend D, Petrinic N (2020) Strain rate and temperature dependent strain localization of a near α titanium alloy". Int J Impact Eng 145:103676
51. Quino G, Tagarielli VL, Petrinic N (2020) Effects of water absorption on the mechanical properties of GFRPs. Compos Sci Technol 199:108316
52. Campbell J, Dowling A (1970) The behaviour of materials subjected to dynamic incremental shear loading. J Mech Phys Solids 18:43–63
53. Lewis J, Campbell J (1972) The development and use of a torsional Hopkinson-bar apparatus. Exp Mech 12:520–524
54. Macdougall D, Harding J (1998) The measurement of specimen surface temperature in high-speed tension and torsion tests. Int J Impact Eng 21:473–488
55. Zhang L, Townsend D, Petrinic N, Pellegrino A (2021) Measurement of pure shear constitutive relationship from torsion tests under quasi-static, medium and high strain rate conditions. J Appl Mech 88(12):121003
56. De Cola F, Pellegrino A, Glößner C, Penumadu D, Petrinic N (2017) Effect of particle morphology, compaction, and confinement on the high strain rate behavior of sand. Exp Mech 58(2):223–242
57. Varley L, Rutherford ME, Zhang L, Pellegrino A (2020) The mechanical response of wet volcanic sand to impact loading, effects of water content and initial compaction. J Dyn Behav Mater 6(3):358–372
58. Casem DT, Zellner MB (2013) Kolsky bar wave separation using a photon doppler velocimeter. Exp Mech 53(8):1467–1473
59. Pan B, Lu Z, Xie H (2010) Mean intensity gradient: an effective global parameter for quality assessment of the speckle patterns used in digital image correlation. Opt Lasers Eng 48:469–477
60. Quino G, Chen Y, Ramakrishnan KR, Martínez-Hergueta F, Zumpano G, Pellegrino A, Petrinic N (2021) Speckle patterns for DIC in challenging scenarios: Rapid application and impact endurance. Meas Sci Technol 32:015203
61. Zhang L, Gour G, Petrinic N, Pellegrino A (2020) Rate dependent behaviour and dynamic strain localisation of three novel impact resilient titanium alloys: Experiments and modelling. Mater Sci Eng A 771:138552
62. Scapin M, Peroni L, Fichera C (2014) Investigation of dynamic behaviour of copper at high temperature. Mater High Temp 31(2):131–140
63. Papasidero J, Doquet V, Mohr D (2014) Determination of the effect of stress state on the onset of ductile fracture through tension-torsion experiments. Exp Mech 54:137–151
64. Dong YP, Tang JC, Wang DW, Wang N, He ZD, Li J, Zhao DP, Yan M (2020) Additive manufacturing of pure Ti with superior mechanical performance, low cost, and biocompatibility for potential replacement of Ti-6Al-4V. Mater Des 196:109142
65. Bai Y, Wierzbicki T (2008) A new model of metal plasticity and fracture with pressure and Lode dependence. Int J Plast 24(6):1071–1096
66. Wierzbicki T, Bao Y, Lee YW, Bai Y (2005) Calibration and evaluation of seven fracture models. Int J Mech Sci 47(4–5):719–743
67. Bao Y, Wierzbicki T (2004) On fracture locus in the equivalent strain and stress triaxiality space. Int J Mech Sci 46(1):81–98
68. Lou Y, Huh H (2013) Extension of a shear-controlled ductile fracture model considering the stress triaxiality and the Lode parameter. Int J Solids Struct 50(2):447–455
69. Korgesaar M (2019) The effect of low stress triaxialities and deformation paths on ductile fracture simulations of large shell structures. Mar Struct 63:45–64
70. Zhou J, Xu Y, Aceves M, Farbaniec L, Patsias S, Macdougall D, Reed J, Petrinic N, Eakins DE, Siviour C, Pellegrino A (2022) The mechanical response of commercially pure copper under multiaxial loading at low and high strain rates. Int J Mech Sci 224:107340
71. Hu LW, Pae KD (1963) Inclusion of the hydrostatic stress component in formulation of the yield condition. J Franklin Inst 275(6):491–502
72. Ehrenstein GW, Erhard G (1994) Designing with plastic: a report on the state of the art. Carl Hanser Verlag report, Munich, Germany
73. Miller E, Dekker M (1996) Introduction to Plastic and Composites: Mechanical Properties and Engineering Applications. New York, USA
74. Drucker DC, Prager W (1952) Soil mechanics and plastic analysis or limit design. Q Appl Math 10(2):157–165
75. Nixon ME, Cazacu O, Lebensohn RA (2010) Anisotropic response of high-purity a-titanium: experimental characterization and constitutive modeling. Int J Plast 26(4):516–553